Biochemistry **2005,** *44,* 9067−9078

Redox-Dependent Structural Differences in Putidaredoxin Derived from Homologous Structure Refinement via Residual Dipolar Couplings[†,‡]

Nitin U. Jain,*[§] Elina Tjioe,[§] Alon Savidor,[||] and James Boulie[§]

Biochemistry, Cellular and Molecular Biology Department and Genome Sciences and Technology Program, University of Tennessee, Knoxville, Tennessee 37996-0840

Received January 26, 2005; Revised Manuscript Received May 1, 2005

ABSTRACT: Structural differences in the [2Fe-2S] ferredoxin, putidaredoxin (Pdx), from the camphor hydroxylation pathway of *Pseudomonas putida* have been investigated as a function of oxidation state of the iron cluster. Pdx is involved in biological electron transfer to cytochrome P450$_{cam}$ (CYP101). Redox-dependent differences have been observed previously for Pdx in terms of binding affinities to CYP101, NMR spectral differences, and dynamic properties. To further characterize these differences, structure refinement of both oxidized and reduced Pdx has been carried out using a hybrid approach utilizing paramagnetic distance restraints and NMR orientational restraints in the form of backbone ^{15}N residual dipolar couplings. Use of these new restraints has improved the structure of oxidized Pdx considerably over the earlier solution NMR structure without RDC restraints, with the new structure now much closer in overall fold to the recently published X-ray crystal structures. We now observe better defined relative orientations of the major secondary structure elements as also of the conformation of the metal binding loop region. Extension of this approach to structure calculation of reduced Pdx has identified structural differences that are primarily localized for residues in the C-terminal interaction domain consisting of the functionally important residue Trp 106 and regions near the metal binding loop in Pdx. These redox-dependent structural differences in Pdx correlate to dynamic changes observed before and may be linked to differences in binding and electron transfer properties between oxidized and reduced Pdx.

Electron transfer is an important event in biological systems and is often controlled via modulation of redox states in proteins. An example of such an electron transfer system is the camphor hydroxylation pathway in the soil bacterium *Pseudomonas putida*. An important component of this pathway is the 106 residue, two iron−two sulfur [2Fe-2S] ferredoxin, putidaredoxin (Pdx),[1] that serves as an electron shuttle between the NADH-dependent flavoprotein, putidaredoxin reductase (PdR), and the heme protein, cytochrome P450$_{cam}$ (CYP101). The role of Pdx is to sequentially transfer two electrons to CYP101 in the catalytic cycle of camphor hydroxylation. The Pdx/CYP101 interaction is one of the best characterized electron transfer couples and has long served as a model system for study of biological redox coupling between [2Fe-2S] ferredoxins and type II cytochrome P450s.

Extensive spectroscopic, kinetic, and thermodynamic data describing the interaction between Pdx and CYP101 is now available, providing insights into the mechanism of electron transfer (*1*−*14*). The electron transfer between Pdx and CYP101 is a tightly regulated redox process involving interconversion of Pdx between the oxidized (Fe^{3+}-Fe^{3+}, Pdx^{o}) and reduced (Fe^{2+}-Fe^{3+}, Pdx^{r}) forms. In two sequential steps corresponding to single turnover of product, Pdx^{o} accepts one electron at a time from PdR and, upon reduction, transfers it to camphor-bound CYP101. The redox-dependent binding to CYP101 is quite specific for Pdx in terms of its effector activity, as evidenced by the drastic reduction in product turnover upon replacement of Pdx with other homologous electron donors (*15*). Redox-dependent differences are also apparent in binding affinities to CYP101, with Pdx^{r} binding oxidized CYP101 with an affinity 100-fold higher than Pdx^{o} (*2*, *3*). This is important in a functional sense since it allows association and dissociation of Pdx during two distinct events of electron transfer, preventing product inhibition. NMR and other biophysical studies indicate that structural and dynamic differences exist between oxidized and reduced forms of Pdx (*1*, *6*, *16*−*22*), which might modulate the binding and electron transfer to CYP101 by Pdx. Considerable importance has been paid to dynamics in Pdx as a source of this modulation. Amide proton exchange rates and comparison of protein backbone dynamics for Pdx^{o} and Pdx^{r} provide evidence for slowing down of protein dynamics upon reduction in several regions of the protein, including regions implicated in binding to CYP101 (*19*, *20*). These dynamic changes with redox state in Pdx were interpreted in terms of a structural entropy model as a

---

[†] This work was supported by a pilot project grant from the Center of Excellence for Structural Biology, University of Tennessee at Knoxville.

[‡] The coordinates for oxidized and reduced putidaredoxin have been deposited in the Brookhaven Protein Data Bank (entries 1YJJ and 1YJI for Pdx^{o} and Pdx^{r}, respectively).

* To whom correspondence should be addressed. Phone: 865-974-4045. Fax: 865-974-6306. E-mail: njain@utk.edu.

[§] Biochemistry, Cellular and Molecular Biology Department, University of Tennessee.

[||] Genome Sciences and Technology Program, University of Tennessee.

[1] Abbreviations: Pdx, putidaredoxin; NMR, nuclear magnetic resonance; RDC, residual dipolar couplings; Adx, adrenodoxin; Pdx^{o}, oxidized putidaredoxin; Pdx^{r}, reduced putidaredoxin; GaPdx, gallium-substituted putidaredoxin; PdR, putidaredoxin reductase; CYP101, cytochrome P450cam; NOE, nuclear Overhauser effect; 2D, two dimensional.

10.1021/bi050152c CCC: $30.25 © 2005 American Chemical Society
Published on Web 06/04/2005

mechanism for coupling oxidation state and binding affinity (*23*). Whether the dynamic changes in certain regions are also overlapped by structural changes requires a detailed analysis of structural differences between the redox forms.

The structure of Pdx^o was first determined using solution NMR spectroscopy (*24*) and later refined using additional NOE restraints (*25*). Paramagnetic metalloproteins often pose a limitation in application of traditional NOE-based NMR approaches due to nonavailability of sufficient restraints in regions affected by paramagnetism. The presence of unpaired electrons in the [2Fe-2S] cluster in both oxidation states at ambient temperature makes the cluster highly paramagnetic. In Pdx^o, the paramagnetic effect of the metal cluster leads to severe line broadening and/or hyperfine shifts of proton resonances located within a radius of 7 Å from the metal cluster, hampering detailed structural analysis of this functionally important region due to lack of structural data. As a result, for structure determination of Pdx^o, the region around the metal cluster had to be modeled on the basis of the crystal structure of a related [2Fe-2S] ferredoxin, bovine adrenodoxin (*26*). Recently, several high-resolution X-ray crystal structures of functional mutant versions of Pdx^o have been published (*27*, *28*). These structures are fairly high resolution, with the structure of the C85S/C73S mutant Pdx^o (1OQQ) showing the best resolution at 1.47 Å. All of the crystal structures are quite similar in overall fold to the NMR structures. These now provide detailed insights into the structural features of the regions surrounding the metal cluster as also other important regions in Pdx^o, offering clues to the redox-dependent function of the protein. However, lack of a high-resolution structure for the functionally important Pdx^r prevents any detailed comparison of structural differences.

Preliminary NMR studies on Pdx^r by Pochapsky and coworkers (*18*) have provided partial structural information by identifying the differences in chemical shifts and NOE restraints between Pdx^o and Pdx^r. These are localized mainly to a region known as the C-terminal cluster region, consisting of residues belonging to a loop region surrounding the metal cluster as well as residues in and around the C-terminus of the protein. It was inferred from these studies that while the overall folds of Pdx^o and Pdx^r did not differ dramatically, the tertiary structural restraints for the C-terminal cluster region did differ. This preliminary structural analysis, although explaining some of the structural differences between Pdx^o and Pdx^r qualitatively, is not sufficient to explain the observed redox-dependent effects and binding differences to CYP101. In an effort to investigate the redox-dependent structural differences in Pdx in detail, we have determined high-resolution solution NMR structures of oxidized and reduced Pdx, helping us to further characterize the relationship between oxidation state and structure/function in Pdx. In doing so, we have developed and applied an approach involving structure refinement of homologous protein structures that utilize paramagnetic distance restraints and NMR orientational restraints in the form of residual dipolar couplings.

Residual dipolar coupling (RDC) measurements in aligned media are increasingly being used in lieu of, or in combination with, traditional NOE-based distance restraints for purposes of biomolecular structure determination. They currently find numerous applications in NMR structure determination protocols, including structural refinement of both small and large proteins, de novo structure determination of small proteins, characterization of interdomain relationships in multidomain proteins, and structure elucidation of protein complexes (*29*−*35*). However, there are few examples in the literature of RDC application for structural refinement of paramagnetic metalloproteins in different redox states, and that too mainly employing self-orientation in external magnetic field from the inherent magnetic anisotropy of the paramagnetic moiety (*36*−*38*). Structure determination of proteins in different redox states offers an excellent opportunity for use of RDC-based methodology since the structure variations between the redox forms are usually small and RDCs are quite sensitive to such variations. If structure for one of the redox forms is available, then a feasible approach for structure determination of the other forms will be to impose RDC restraints measured for them onto the closely related known structure to determine the unknown structures. We demonstrate this methodology in high-resolution structure determination of Pdx^o and Pdx^r, starting from the known lower resolution NMR structure and converting it to the new structures using RDC restraints measured in external orienting media for Pdx^o and Pdx^r.

Paramagnetism of the metal cluster precludes use of this methodology in the immediate region surrounding the metal cluster within a radius of 7 Å. One of the approaches frequently used for structural interpretation of residues in the paramagnetic region is to calculate a distance between a nucleus and metal center from paramagnetic contributions to nuclear relaxation (*39*, *40*). Recently, sequence-specific NMR assignments and distance restraints from enhancements in relaxation times for backbone ^{13}C′, ^{15}N heteronuclear resonances within the paramagnetic region of both Pdx^o and Pdx^r have been reported (*23*, 41), making it possible to develop a hybrid approach that combines the paramagnetic and orientational information. Here, we present refined solution NMR structures for both oxidized and reduced Pdx obtained using this hybrid approach and describe the structural features in the regions undergoing conformational changes between the two redox forms. Our results indicate redox-dependent structural differences in Pdx that correlate to previously observed dynamic changes and may be linked to differences in binding and electron transfer properties between Pdx^o and Pdx^r.

MATERIALS AND METHODS

Sample Preparation and NMR Spectroscopy. Expression and purification of ^{15}N-labeled Pdx followed published protocols (*25*). Plasmids for expression of Pdx were kindly provided by Dr. Thomas Pochapsky (Brandeis University). After purification, samples of Pdx were concentrated and dialyzed against NMR sample buffer (50 mM Tris-HCl, pH 7.4, 50 mM KCl, 90% H_2O:10% D_2O) before being used for the NMR experiments. Typical NMR samples had a concentration range from 1 to 2 mM. Samples of Pdx^r were prepared anaerobically by reduction of Pdx° using methods described previously (*23*).

All NMR experiments were carried out on a Varian Unity Inova 600 MHz spectrometer. RDC measurements on both Pdx^o and Pdx^r were carried out in an identical fashion. Different alignment media, bicelles, and phage were used for RDC measurements. Two sets of data in 5% (w/v) bicelle solution (DMPC:DHPC, 2.9:1) were collected: a data set at 25 °C corresponding to the isotropic phase of bicelles and a data set at 29 °C corresponding to the aligned phase of the bicelles. For measurements in phage, a sample of Pdx was prepared in the absence and presence of 10 mg/mL Pf1 phage (Asla Ltd., Latvia) corresponding to the isotropic and aligned phase for measurements. ^{1}H$-$^{15}N couplings were measured for each sample at 25 °C from a two-dimensional sensitivity-enhanced HSQC experiment coupled in the ^{15}N dimension (*42*). RDCs were extracted as a difference in splitting between the isotropic and aligned phase. For each NMR experiment, a total of 1024 × 256 complex data points were collected in the direct and indirect dimensions, respectively, followed by linear prediction and zero filling to a final data set of 1024 × 1024 complex data points. Typically, a sweep width of 8000 Hz for the directly detected proton dimension and 1800 Hz for the indirectly detected dimension was employed, resulting in a 1.7 Hz/point resolution for the coupled dimension. ^{1}H chemical shifts in spectra were referenced against external DSS using the water signal as an internal reference. ^{15}N chemical shifts were referenced to external liquid ammonia using the ^{1}H resonance of H_2O. All sets of data were processed and analyzed using the Felix software package (Molecular Simulation Inc.). For RDC data analysis, sequence-specific backbone ^{15}N$-$^{1}H assignments for Pdx^o and Pdx^r published previously were used (*25*).

Structure Calculation. Structural calculations for Pdx^o and Pdx^r were performed on a Silicon Graphics Octane workstation using the simulated annealing protocol in XPLOR-NIH (*43*). The Fe_2S_2 metal cluster was modeled into the protein initially using bond geometry and distance restraints for the metal cluster and ligating cysteines obtained from the crystal structure of Adx (*26*). As summarized in Table 1, a total of 1271 NOE distance restraints, 160 dihedral angle restraints, and 155 RDC restraints were used for structure refinement of Pdx^o. Structure refinement of Pdx^r was carried out with 1273 NOE distance restraints, 160 dihedral angle restraints, and 150 RDC restraints. The NOE and dihedral angle restraints are similar to the restraints used for calculation of the previous 1PDX structure and were retrieved from BioMagResBank. The previous NMR structure calculation utilized restraints from gallium-substituted Pdx (GaPdx) in addition to the Pdx restraints (*18, 39*). In the current calculation, all modeling restraints from GaPdx were removed so as not to bias the calculated structure toward structural features in GaPdx. Due to considerable sequence homology in the metal binding region and overall structural and functional homology with Adx, dihedral angle restraints for backbone ϕ, ψ angles in the metal binding region (residues 38−48, 85−86) and side chain χ_1 angles for the four ligating cysteines from the Adx structure (1AYF) were retained for modeling. The backbone dihedral angles ϕ and ψ for the paramagnetic residues were modeled with a range of ±40° and ±60° for Pdx^o and Pdx^r respectively, allowing for conformational flexibility around the metal center. In Pdx^o, all interresidue NOEs to the side chains of Tyr 33 and the C-terminus residue Trp 106 that exhibit strong local dynamics were removed to allow them to orient under the influence of RDCs (*vide infra*). These NOEs were absent in Pdx^r calculations as well, except for cases where a strengthening of a particular NOE was observed upon reduction (e.g., Val 74 H$^\gamma$$-$Trp 106 H$^\epsilon$). Changes in NOE patterns for other residues in the diamagnetic region upon reduction have been detailed previously (*18*). These changes were additionally incorporated for structure refinement of Pdx^r. The complete restraint set for the diamagnetic region is described in Table 1. In the paramagnetic region, a total of 28 distance restraints derived from paramagnetic relaxation enhancements and corresponding to distances between Fe atoms and backbone ^{15}N and ^{13}C′ atoms in residues affected by paramagnetism (residues 38−48, 85−87) were used during the structure refinement calculations (see Supporting Information). Sequence-specific assignments for backbone ^{13}C′ (carbonyl) and ^{15}N resonances of Pdx^o and Pdx^r have been made previously for these residues using double-labeled samples and selective difference decoupling experiments (*41*). The distances in both Pdx^o and Pdx^r were allowed a variation of ±0.8 Å.

RDCs were included in the refinement as restraints with estimated measurement errors of 2 Hz in bicelles and 1.5 Hz in phage for Pdx^o, while for Pdx^r they were 1.5 and 1.0 Hz, respectively. Fitting of RDC data to the crystal structure of the C73S/C85S Pdx^o (1OQQ) using the program MODULE (*44*) gave estimates for the initial values of axial and rhombic components of the alignment tensor in bicelles ($D_a = -10.2$ Hz, $R = 0.15$) and phage ($D_a = -6.1$ Hz, $R = 0.38$) for structure calculations. This fit was deemed reliable on the basis of the excellent correlation observed between measured RDCs and back-calculated RDCs from the crystal structure in the correlation plot for Pdx^o (Figure 2A). The estimated axial and rhombic values were then input as starting values during the structure refinement process of Pdx^o. The values of D_a and R were further optimized using the method of Clore et al. (*22*). For Pdx^o, preliminary calculations were run with R values in the range 0.11−0.21 in steps of 0.02 and D_a values in the range −8.0 to −12.0 in steps of 0.2 corresponding to bicelle medium. The optimum values were selected on the basis of the parameters that gave the lowest energy structure, and their values correpond to $D_a = -9.5$ Hz, $R = 0.19$. The optimum values for phage were similarly found to be $R = 0.48$ in a range of $R = 0.33$ to $R = 0.52$ and $D_a = -5.5$ Hz in the range −4.5 to −6.5 Hz. For Pdx^r, a similar optimization protocol was followed, and optimum values for bicelles were found to be $R = 0.24$ in a range of $R = 0.15-0.27$ and $D_a = -4.7$ Hz in the range −4.5 to −6.5 Hz, while the optimum values for phage were found to be $R = 0.43$ in a range of $R = 0.33-0.52$ and $D_a = -2.8$ Hz in the range −2.5 to −4.5 Hz.

Structures were calculated via simulated annealing in torsion angle space, starting with coordinates from the previously reported NMR structure of Pdx^o (1PDX) within the program X-PLOR-NIH (*43*). A square-well pseudopotential for RDC restraints was used in the target function. Refinement via simulated annealing incorporating low-temperature stages was carried out in two steps using a general protocol described by Chou et al. (*45*): a low-temperature cooling step from 200 to 10 K in steps of 10 K, followed by Verlet dynamics for a period of 10 ps in steps of 2 fs, and final minimization over 50 cycles in 250 steps. During the cooling stage, the NOE restraints were scaled down using a scaling factor from 20 to 0.2 kcal mol^{-1} Å^{-2}, while the RDCs were ramped up from 0.0001 to 2.0 kcal mol^{-1} Å^{-2} for bicelles and 1.5 kcal mol^{-1} Å^{-2} for phage, respectively. The backbone dihedral angle force constants

Table 1: Structural Statistics for the Calculated Ensemble of Pdx Structures

	Pdx^o	Pdx^r
distance restraints		
NOE restraints in diamagnetic region	1271	1273
metal restraints	28	28
hydrogen bond restraints	36	37
dihedral angle restraints		
total	160	160
ϕ	94	94
ψ	14	14
χ	44	44
ligating cysteines from X-ray	8	8
residual dipolar coupling restraints (total)		
total	155	150
5% DMPC:DHPC (2.9:1.0)	77	75
10 mg/mL phage	78	75
restraint violations		
NOE (>0.5 Å)	15	13
dihedrals (>5°)	0	0
dipolar couplings		
bicelle (>3 Hz)	0	0
phage (>2 Hz)	0	0
structural quality and coordinate precision		
backbone RMSD to		
mean (Å) residues 1−106	0.3	0.7
mean (Å) secondary structures	0.1	0.3
X-ray (1OQQ) (Å) residues 1−106	1.2	1.6
X-ray (1OQQ) (Å) secondary structures	0.8	1.0
% of residues in Ramachandran plot		
most favored regions	83.7	80.3
additionally allowed regions	15.9	19.4

were also scaled down from 300 to 50 kcal mol^{-1} Å^{-2} over the course of the cooling. Fifty structures were generated each for Pdx^o and Pdx^r, having no violations greater than experimental errors for the dipolar couplings, out of which a cluster of 15 lowest energy structures for Pdx^o and 11 lowest energy structures for Pdx^r was selected for analysis. The structures were checked by PROCHECK (*46*) for consistency of stereochemistry and bond geometry. An individual conformer with lowest RMSD to the mean was selected as a representative structure for comparison purposes in each case. The conformational restraints used for calculating the structures and coordinates for the structural ensemble have been deposited in the Protein Data Bank with accession numbers 1YJI (Pdx^r) and 1YJJ (Pdx^o).

RESULTS

Measurement of Residual Dipolar Couplings and Structure Refinement. $^1D_{NH}$ backbone residual dipolar couplings were measured on a ^{15}N-enriched sample of oxidized and reduced Pdx partially aligned in bicelle and Pf1 phage media. As detailed in Table 1, a total of 155 $^1D_{NH}$ couplings for Pdx^o and 150 $^1D_{NH}$ couplings for Pdx^r were obtained in both media, excluding degenerate and ambiguous data. This represents most of the residues observable in the diamagnetic region of Pdx. In Pdx^r, there is loss of some RDC data relative to Pdx^o due to increased paramagnetic effects for residues 23, 50, 71, and 88. Slight broadening is also observed for residues 66−67. This is due to an increase in the radius (ca. 8 Å) around the metal cluster affected by line broadening, resulting from a larger manifold of unpaired electron states populated at room temperature in Pdx^r.

Figure 1 shows selected regions from the two-dimensional ^{15}N-coupled spectra depicting RDC measurements for a set of residues in Pdx in the two aligned media. Owing to good alignment of Pdx in both media, the spread of measured RDCs is reasonably large (−22 Hz to +15 Hz in bicelles and −14 Hz to +10 Hz in phage for Pdx^o), and with most resonances being well separated, RDC measurements were obtained with considerable accuracy. The quality of the acquired data is illustrated via a correlation plot (Figure 2A) between experimental RDCs for Pdx^o and back-calculated RDCs from the 1.47 Å crystal structure of the C73S/C85S mutant Pdx^o (1OQQ). Good agreement is observed between experimentally measured RDCs and the crystal structure, with only few measurements (residues 8, 23, 26, 56−58, 74, 103, and 106) falling outside experimental error limits. Similar behavior is observed for RDCs measured in phage medium (see Supporting Information), except some additional residues (residues 16−18, 33, 55, 63, 88, 93, and 96) fall outside the fit. Most of these residues are present in fairly dynamic regions of the protein as suggested by prior studies involving backbone dynamics (*20*) and are thus likely to exhibit small structural deviations from the crystal structure resulting from dynamic averaging of RDCs. In comparison, the correlation plot obtained using the refined NMR structure (1PDX) shows poor fit of the RDC data in all regions of the protein, indicating a lower quality for this structure (Figure 2C).

Figure 3 shows the distribution of measured RDCs in bicelle medium for residues in the diamagnetic region in oxidized versus reduced Pdx. The overall RDC distribution is quite similar for both redox forms. However, one can see individual changes in RDC values outside of experimental error limits. These are mainly localized to regions consisting

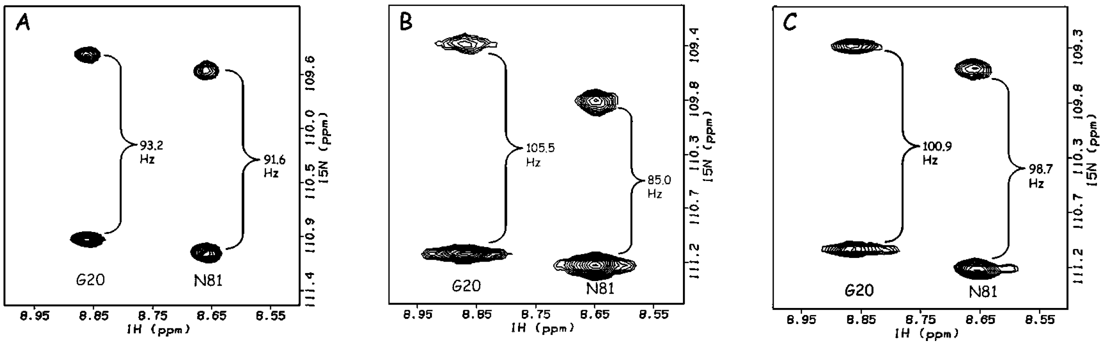

FIGURE 1: Residual dipolar coupling measurements for a representative set of resonances in spectra recorded using a ^{15}N-coupled HSQC sequence at 600 MHz on a ^{15}N-labeled sample of Pdx^o (50 mM Tris-HCl, pH 7.4, 50 mM KCl, 90% H_2O−10% D_2O). (A) Isotropic solution, (B) aligned in 5% DMPC:DHPC (2.9:1.0) bicelle solution, and (C) aligned in 10 mg/mL phage solution. $^1D_{NH}$ RDC values are measured from the difference in peak splittings (shown in hertz).

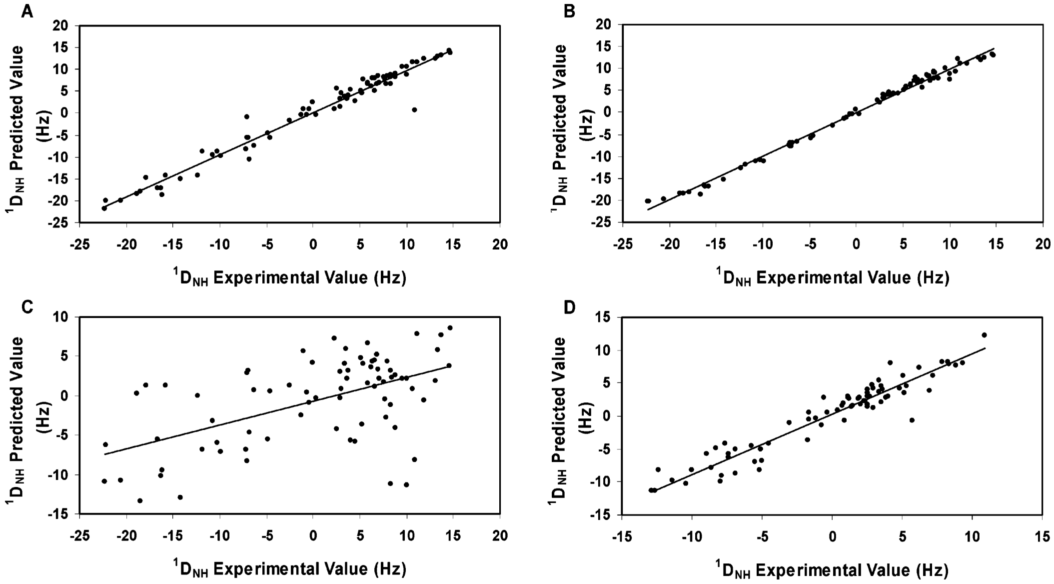

FIGURE 2: Correlation plot of experimentally measured $^1D_{NH}$ RDCs in bicelle solution versus back-calculated values for Pdx. (A) Crystal structure (1OQQ) fit to RDCs measured for Pdx^o (correlation coefficient $R^2 = 0.96$), (B) RDC-refined structure fit to RDCs measured for Pdx^o (correlation coefficient $R^2 = 0.99$), (C) 1PDX structure fit to RDCs measured for Pdx^o (correlation coefficient $R^2 = 0.30$), and (D) crystal structure (1OQQ) fit to RDCs measured for Pdx^r (correlation coefficient $R^2 = 0.91$). RDCs used in the plot were measured with an estimated precision of ±1.5 Hz.

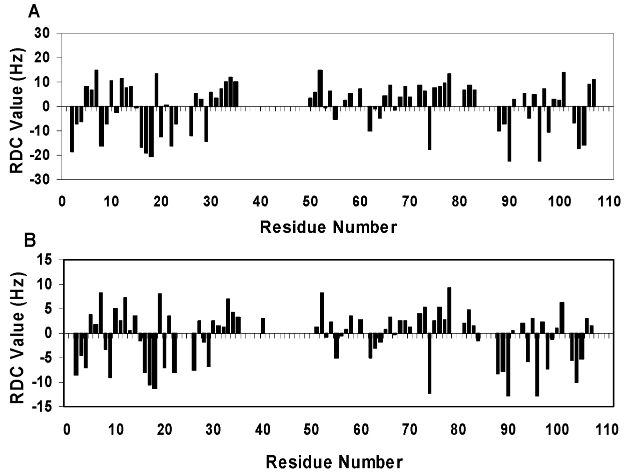

FIGURE 3: Plot of $^1D_{NH}$ residual dipolar coupling values versus residue number measured in 5% DMPC:DHPC (2.9:1.0) bicelle solution for (A) Pdx^o and (B) Pdx^r. The couplings were measured with an estimated precision of ±1.5 Hz.

of His 8–Thr 11, Asp 16–Val 21, Asn 30–Ile 35, Glu 54–Glu 65, Cys 73–Leu 78, Ile 88–Ile 89, and the C-terminal residues Asp 103–Trp 106. The similarity in distribution pattern and individual residue differences is retained in phage media, indicating local structural changes while maintaining overall global fold upon change in oxidation state. Our RDC results are thus in line with results obtained from previous NMR studies where no redox-dependent chemical shift or NOE intensity changes were observed for the majority of the residues in the diamagnetic region (*18*). The only regions where chemical shifts and NOE differences were significantly apparent include His 8, Ser 22, Val 28–Ile 35, portions of the α-helix extending from Glu 65 to Cys 73, the loop Val 74–Leu 78, which connects the helix to the Lys 79–Ser 82 type I turn, Gln 87–Ile 88, and the C-terminal residues Pro 102–Trp 106. On the basis of inspection of distances of these residues from the metal cluster, most of these residues are well outside the paramagnetic sphere of influence of the metal cluster to rule out any significant pseudocontact shift contributions.

Apart from dipolar coupling measurements, refinement of protein structure utilized NOE, dihedral angle, and hydrogen bond restraints that were included as described in the Materials and Methods section. For the refined structure ensemble of Pdx^o generated previously without RDC data (1PDX), 58.8% and 41.0% of defined backbone ϕ, ψ values for all non-glycinyl residues were mapped to the most favored regions and additionally allowed regions of the Ramachandran plot (*46*). The corresponding values are improved to 83.7% and 15.9%, respectively, for the ensembles generated with RDC restraints. In Pdx^r, the corresponding values are 80.3% and 19.4% respectively. A correlation plot of experimental versus back-calculated RDCs for the RDC-refined structure shows the extremely good fit of a representative structure in the ensemble to the measured RDCs, validating use of this structure refinement approach (Figure 2B).

Comparison of RDC-Refined Structure with Previous Solution NMR Structure and Crystal Structures of Oxidized Pdx. The set of structures generated with RDC restraints is somewhat better converged than the previously refined NMR structures (1PDX); the backbone and heavy atom RMSD values are 0.3 and 0.6 Å respectively (0.2 and 0.5 Å for the diamagnetic region alone), compared to 0.5 and 0.8 Å for the structures without RDC restraints. The observed improvements result from the better defined relative orientations of the two major helices (helix D and helix G) and β-sheets (A and B) as also some of the loop regions. As can be seen from the comparison with the C73S/C85S mutant crystal structure (1OQQ) in Figure 4, the new RDC-refined structure for Pdx^o is now closer to the crystal structure in overall backbone fold compared to the previous NMR structure (overall backbone RMSD of 1.2 Å compared to 2 Å previously). Since the RMSD between the secondary structure elements of the RDC-refined structure and crystal

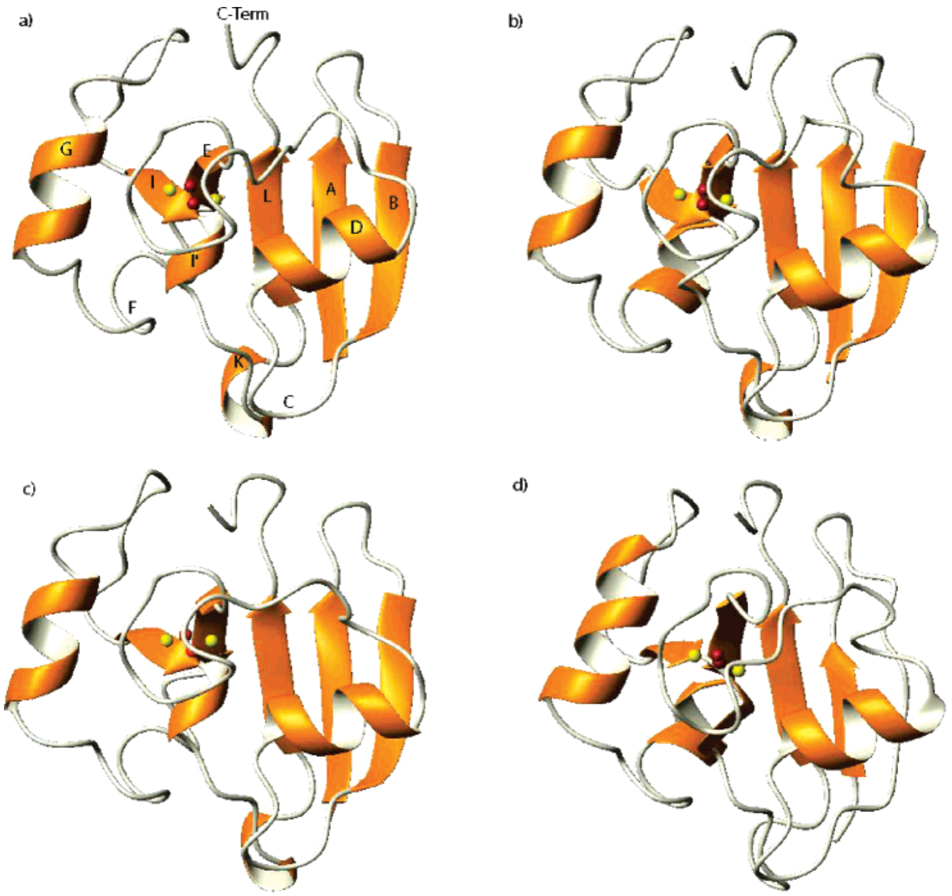

FIGURE 4: Ribbon representation of the (a) crystal structure (1OQQ) of Pdx^o, (b) RDC-refined structure of Pdx^o, **(**c) RDC-refined structure of Pdx^r, and (d) previous NMR structure of Pdx^o (1PDX). The different structural elements of Pdx are labeled with letters A−L as described in ref *20*. The label C-term stands for C-terminus of the protein. The [2Fe-2S] metal cluster is shown as spheres. The figures were prepared using the program MolMol (*64*).

structure is quite low (0.8 Å) (Table 1), the majority of the RMSD results from differences in loop structures, especially the region comprised of residues Gly 31−Val 36 that is at the beginning of the metal binding region. In the 1PDX structure ensemble, this region exhibits considerable conformational heterogeneity in solution that is also retained to some extent in the current set of structures. The observed heterogeneity may be due to a combination of several factors. For one, there are few interresidue NOE contacts for residues in this region with the rest of the protein. Second, this region is known to possess the highest mobility in the entire molecule, as demonstrated by previous dynamic studies on Pdx. This has implications for redox-dependent function, as discussed in the next section. Even in the 1OQQ crystal structure, this region along with the C-terminal region was found to exhibit the highest *B*-factor values in the three independent molecules of the crystal form, indicating considerable flexibility in this part of the molecule. Not surprisingly, this region displays a different conformation in a recently published second crystal structure of the C73G mutant Pdx (1R7S) (*28*).

In terms of other significant structural differences for this region, the side chain of Tyr 33 is only partially solvent exposed in the majority of our structures as in the previous NMR structure, in contrast to the crystal structure where it is completely solvent exposed. In the previous structure calculation of 1PDX, most of the interresidue NOE contacts for Tyr 33 were derived from the measurement of GaPdx and were likely biased toward the GaPdx structure in its side chain orientation (*25*, *47*). To alleviate the bias, all interresidue NOEs to the side chain were removed and Tyr 33 was allowed to adopt conformations based on the backbone RDCs. A range of conformations averaging around a side chain orientation only slightly exposed to the solvent was still found in our case. Interestingly, in another recently published crystal structure of the C73G mutant Pdx (1R7S), the side chain of Tyr 33 is found in a conformation intermediate between our structure and the 1OQQ structure. It is likely that the side chain of Tyr 33 is sampling a range of conformational states as part of mobility in this region, leading to observation of the different conformations. Other minor structural differences between the current structure and the crystal structure are observed for residues Gly 20−Val 21 in the loop region C connecting strand B of the β-sheet and helix D as also the extended loop comprising residues Ala 55−Ala 63. These regions contain some of the residues with lowest order parameters in Pdx (*19*, *20*), so it is not surprising to see higher RMSD between the structures in this region on account of mobility.

Use of paramagnetic distance restraints from backbone carbonyl and nitrogen atoms to the metal center for residues Asp 38−Cys 48 has also improved the structure of the metal binding loop compared to 1PDX. The metal binding loop is now conformationally similar to that observed in the crystal structures with the metal center and cysteine ligands occupying almost identical positions. Comparison with the

1OQQ crystal structure indicates that the paramagnetic distance restraints used in our calculation match quite well within experimental error with the distances observed in the crystal structure (see Supporting Information). As a result, the loop retains some of the important structural features observed in the crystal structure. The side chains of Thr 47 O^{γ}H−Cys 45 S^{γ} and Ser 42 O^{γ}H−Ser 44 O^{γ}H are within hydrogen-bonding distances similar to that in the crystal structure. A key interaction between the carbonyl group of Ser 44 and the carboxyl group of Asp 38 that helps to stabilize the metal binding loop is also now observed. The hydrogen-bonding pattern around another key residue, His 49, is also preserved in our structure. His 49 is conserved in plant and vertebrate-type [2Fe-2S] ferredoxins and has been suggested to act as a mechanical linker in transmitting redox-dependent conformational changes from the metal binding loop to the C-terminal cluster region (*48*, *49*). The imidazole ring of His 49 is within hydrogen-bonding distances of residues Ser 82, Ala 76, and Arg 104 that are part of the C-terminal cluster and can likely interact via intermediate water molecules observed in the crystal structure. The observation of these key interactions illustrates the success of our hybrid approach in reproducing detailed structural features around paramagnetic [2Fe-2S] centers using minimal orientational and distance data like those used here.

One of the more functionally important regions in Pdx other than the metal binding loop is a region known as the C-terminal interaction domain consisting of the C-terminal residues Gln 105−Trp 106, residues His 49, Tyr 51, and Val 74−Ser 82. While His 49, Tyr 51, and Ser 82 are involved in a stabilizing hydrogen-bonding network around the metal cluster, site-directed mutagenesis studies have highlighted the importance of Trp 106 in the binding interaction of Pdx with CYP01 (*41*). Modification of Trp 106 with a nonaromatic residue greatly reduces the binding affinity, in turn affecting the electron transfer to CYP101. The side chain of Trp 106 has been shown to be fairly dynamic from both NMR dynamic studies and fluorescence quenching studies (*20*, *49*, *50*), sampling multiple conformational states. Similar conformational heterogeneity is observed in our RDC-refined ensemble just as in the 1PDX structure ensemble. However, the average conformation of the side chain places it away from other residues in the interaction domain in parallel with the conformation observed in the crystal structure. In cases with strong motional effects such as in Pdx^o, the averaged RDC selects a conformation that is sampled quite frequently in solution and is similar to the one represented in our structure. We note here that, even in the crystal structures, the side chain of Trp 106 has been crystallized in different conformations in different crystal forms of the protein, again pointing to the conformational mobility of this residue.

Structural Comparison between Oxidized and Reduced Pdx. The structure refinement of Pdx^r was carried out in manner similar to Pdx^o, utilizing paramagnetic and RDC restraints measured for Pdx^r. As can be seen from Figure 4c, there are no major conformational changes in the protein as a response to redox state. The reduced structure retains all major secondary structure elements observed in Pdx^o. However, there are some changes in the arrangement of these elements relative to Pdx^o. The largest change is observed for helix D that is now displaced relative to its position in Pdx^o by extension of region Gly 31−Asp 38 connecting the helix and metal binding loop. As a result of this movement, the loop region C consisting of residues Asp 19−Val 21 moves closer toward helix K, twisting strand B from the central β-sheet region in the protein and in turn affecting the conformation of residues His 8−Thr 11. On the C-terminal side of the protein, helix G is also slightly displaced from its position, moving away from the metal binding region (ca. 1 Å) by extension of loop Lys 59−Asn 64 accompanied by structural changes in the C-terminal interaction domain. Most of the residues in the loop Lys 59−Asn 64 exhibit some of the lowest order parameters in Pdx^o that increase dramatically in Pdx^r, signifying reduction in dynamic character of this loop. Extension of this loop might be a way of achieving this.

The region with highest RMSD to the Pdx^o structure (RMSD > 3 Å) involves another loop region, Gly 31−Asp 38, that is located at the start of the metal binding region. This region shows considerable flexibility and conformational heterogeneity in solution in both Pdx^o and Pdx^r structures, with lowest order parameters for the two residues Tyr 33 and Asp 34 (*10*). In Pdx^r, this region becomes less dynamic, resulting in an increase in order parameters for Tyr 33 and Asp 34. The structure of Pdx^r may help to explain, in part, this observation. The region in Pdx^r containing these two residues is now extended relative to the Pdx^o structure and closer to His 8−Thr 11, making it conformationally more restrictive and thus less dynamic. This change in conformation causes the side chain of Tyr 33 to be slightly more buried than in the Pdx^o structure, reducing its motion, while at the same time exposing the side chain of Asp 34 to the solvent. Site-directed mutagenesis has implicated Asp 34 as one of the residues important in binding interactions with CYP101 via salt bridge formation with a basic residue in CYP101 (*51*). This structural change in the side chain of Asp 34 can increase the possibility of such an interaction, making Pdx^r bind tighter to CYP101. Another important residue implicated in binding interactions and also electron transfer to CYP101 by site-directed mutagenesis studies is Asp 38, the other aspartate residue in this region (*51*). There is no significant change for the side chain of Asp 38. It is still solvent-exposed, except that it now points toward the C-terminus carboxylic group of Trp 106 and is closer to Thr 47 that is involved in hydrogen-bonding interaction with one of the ligating cysteines, Cys 45 (Figure 5). Interaction of side chain of Asp 38 with Thr 47 may help to stabilize the delocalization of unpaired electron density and subsequent electron transfer, thus explaining its importance.

Further inspection of the Pdx^r structure identifies several other regions in the protein that show distinct structural differences. Among these include portions of helix G from Glu 65−Cys 73, where the region around Arg 66−Glu 67 is observed to undergo slight extension. Differences are also observed for Val 74−Thr 75 and the Lys 79−Ser 82 type I turn that are now slightly closer to the metal cluster. We note that chemical shift changes are also observed for most of the above residues upon reduction. Some of these residues are part of the C-terminal interaction domain. Ser 82 is involved in a hydrogen-bonding network in this region with His 49 and Tyr 51. Slight changes in the hydrogen-bonding pattern are manifested in the form of lengthening of the distance between Ser 82 O^{γ} and $N^{\epsilon}1$ of His 49 and shortening

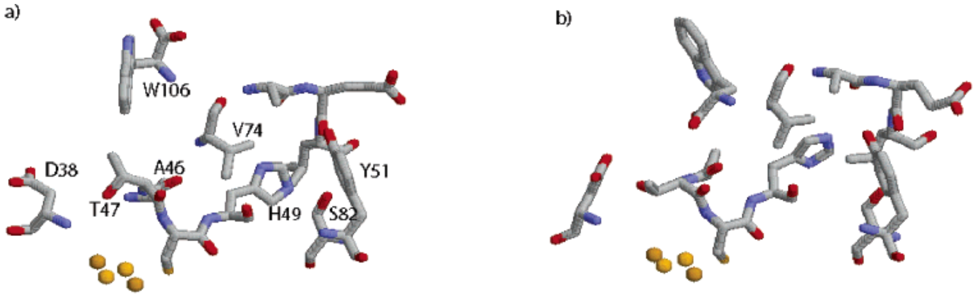

FIGURE 5: Structural differences in the C-terminal interaction domain between (a) Pdx^{o} and (b) Pdx^{r}. Redox-dependent differences in key interactions between the side chains of His 49, Tyr 51, and Ser 82, side chains of Trp 106, Ala 46, and Val 74, and side chains of Asp 38 and Thr 47 are illustrated. The [2Fe-2S] metal cluster is shown as spheres. The figure was prepared using the program RasMol (*65*).

of the distance between His 49 N$^{\epsilon}$2 and Tyr 51. This change might be partly responsible for mechanically transmitting the effects of change in oxidation state of the metal cluster to the C-terminal interaction domain, as has been suggested previously.

The C-terminal cluster region in Pdx^{r} is also now more compact (Figure 5) than in Pdx^{o} due to movement of Val 74 toward the metal cluster and the Trp 106 side chain into the region adjacent to the metal center forming a tight hydrophobic pocket comprising residues Val 74–Ala 76, Ala 46, and Trp 106. The side chains of Ala 46 and Val 74 are in close proximity to the indole ring of Trp 106, likely involved in hydrophobic interaction. The side chain of Ala 46 is also now closer to the indole ring of Trp 106 compared to its position in Pdx^{o}. Interresidue NOEs have been observed for both of the side chains with the indole ring of Trp 106 that get strengthened in Pdx^{r}. We interpret this structural rearrangement in Pdx^{r} as restricting the range of motions experienced by the side chain of Trp 106 in Pdx^{o}, making it sample conformational states preferentially in proximity to the side chains of these residues. This agrees very well with the observed changes in dynamics between Pdx^{o} and Pdx^{r} in this region, which had suggested narrowing down of conformational motion in this region upon reduction. This would allow better interaction with similar aromatic residues in CYP101 overcoming the loss of entropy due to restricted motion and explaining the role of this residue in modulating the binding interaction with CYP101.

Finally, small structural differences are also noticeable within the metal binding region. Paramagnetic distance restraints from relaxation rate measurements for hyperfine-shifted backbone ^{15}N, ^{13}C′ resonances and dihedral angle modeling restraints from Adx structure have been used to loosely constrain the placement of the loop region around the metal cluster. The region around the metal cluster consists of four conserved cysteine residues (Cys 39, Cys 45, Cys 48, and Cys 86) that ligate the [2Fe-2S] metal cluster. Two of the cysteines, Cys 39 and Cys 45, ligate one Fe atom (Fe1), while the other two, Cys 48 and Cys 86, ligate the other Fe atom (Fe2). Recent crystal structures of Pdx^{o} reveal the presence of hydrogen bonds between the backbone nitrogen of Ser 44 to S$^{\gamma}$ of Cys39 and the backbone nitrogen of Thr 47 to S$^{\gamma}$ of Cys 45. Thr 47 is a residue that is conserved in several [2Fe-2S] ferredoxins and likely important in delocalization of unpaired electron density from the metal cluster via the hydrogen bond. Interestingly, ^{15}N and ^{13}C′ hyperfine-shifted resonances of Ser 44 and Thr 47 show significant chemical shift changes and temperature dependencies as a function of oxidation state (*23*). Upon reduction, the ^{15}N resonances for these two residues show increased relaxation rates as do the ^{15}N resonances of Cys 39, Cys 45, Cys 48, and Cys 86, indicating a shortening of distances between their backbone nitrogen atoms and the metal cluster. On the other hand, the ^{15}N resonances of Gly 41, Ala 43, and Ala 46 relax more slowly, and their chemical shifts move toward the diamagnetic region of the spectrum upon reduction. We interpret these changes as small, localized structural changes around the metal center, causing the loop to constrict around Cys 39 and Cys 45 due to shortening of hydrogen bonds between Ser 44–Cys 39 and Thr 47–Cys 45. As a result, these residues and the ligating cysteines move closer to the metal cluster, while Gly 40–Ala 43 moves away, causing a slight deformation of the loop at Gly 40–Ala 43. The flexible nature of Gly 40–Gly 41 has been suggested to play a crucial role in controlling the redox-dependent dynamic effects of Pdx, as observed by slowing down of conformational exchange upon restriction of this movement via replacement of Gly 40 with more bulky, rigid residues (*23*). Results from our structure calculation of Pdx^{r} support this observation.

Comparison of RDC-Refined NMR and X-ray Crystal Structures of Reduced Putidaredoxin. While this paper was under review, the X-ray crystal structures of C73S and C73S/C85S mutants of reduced putidaredoxin also appeared in the literature (*66*). At the same time, the crystal structures of oxidized putidaredoxin were reevaluated under new conditions that prevented photoreduction of the crystalline C73S and C73S/C85S mutants during X-ray data collection. Overall, there is good agreement between the X-ray crystal structures of mutant Pdx^{r} and the refined NMR structure of wild-type Pdx^{r} reported here. Just as in the case of Pdx^{o}, observed differences between the NMR and crystal structures for Pdx^{r} again correspond mainly to regions known to be fairly flexible, such as helices D and G, and the loop regions immediately following and preceding these helices. This is not surprising since high RMSD is also observed for these regions in the crystal structures, particularly in the loop regions. Extension of these loop regions (55–64, 30–35) apparent in our Pdx^{r} structures is similar in nature to a slight redox-dependent motion of two distinct lobes of Pdx (residues 1–35, 52–61, 85–101 and residues 36–51, 62–84, and 102–106) detected between the oxidized and reduced crystal structures.

Structure analysis of the corrected oxidized models with the reduced mutant crystal structures revealed that the carbonyl oxygen of Cys 45 in the Cys 45–Ala 46 peptide bond flips from an "in" conformation in Pdx^o to an "out" conformation in Pdx^r. Such a flip is not observed in our structure, where the carbonyl oxygen is predominantly in an "in" conformation. It is not clear at this point whether this discrepancy arises due to mutation of the redox-sensitive Cys 73 residue that is hydrogen-bonded to Met 70, which is in turn interacting with the carbonyl oxygen of Cys 45, or due to lower resolution of the paramagnetic distance data used for residues around the metal cluster in Pdx^r. Aside from this, there are no significant structural differences for other residues in the metal binding loop between the NMR and crystal structures, since similar hydrogen-bonding patterns are maintained in the two redox forms. An exception is the flexible residue Gly 40, which is found to be at a larger distance from the metal center in the NMR structure than the crystal structures. Tightening of the upper part of the metal binding loop in the crystal structures of Pdx^r is similar to that observed in our NMR structure.

In the region preceding the metal binding loop (Gly 31−Asp 38), the presence of multiple conformations is apparent in the crystal structures as is also the case in the NMR structures. Increased interaction between the peptide fragment Ile 32−Ile 35 with Ser 7−Asp 9 and Pro 102−Asp 103 is observed; however, the extent of these interactions and conformational changes differs in different molecules in the crystal lattice. The only residue with no major redox-dependent conformational change is the functionally important residue Asp 38, in line with the NMR structure. From the crystal structure data, it was concluded that redox-dependent structural rearrangement of Tyr 33 and Asp 34 might play an important role in transmitting the redox signal from the active site to the neighboring residues via stabilizing hydrogen-bonding interactions. This ties in well with the NMR studies of Pochapsky and co-workers (*23*), which suggest that the metal binding loop in Pdx consisting of the flexible residues Gly 40 and Gly 41 is the primary determinant of redox-dependent conformational selection and changes in dynamics. Tightening of the metal binding loop can lead to the rearrangement and stabilization of surrounding residues in Pdx^r via these flexible residues, thus modulating the redox-dependent binding to CYP101.

DISCUSSION

Direct structure refinement against RDC restraints has been applied to other protein systems before (*30*, *52*−*54*). In all cases, application of RDC constraints has resulted in substantial improvement in the rate of convergence and quality of protein structures. Use of RDCs in addition to NOE restraints overcomes some of the shortcomings of the NOE-based approach, such as poor definition of regions due to lack of sufficient long-range NOE contacts. In our case, upon incorporation of RDC restraints, we have noticed remarkable improvement in the structure of Pdx^o over the structure reported previously without RDC restraints, especially in the definition and relative orientation of secondary structure elements and regions adjacent to the metal binding loop including the C-terminal cluster region. The improvements are reflected in the increased agreement of experimental restraints and improved quality of the Ramachandran plots.

While RDC-based approaches aimed at refining structures based on structural homology have been described before (*45*), highly paramagnetic regions in proteins such as Pdx remain inaccessible to acquisition of RDC restraints owing to more efficient relaxation of nuclei compared to the time needed for *J*-couplings to evolve. For such regions, use of distance restraints from paramagnetic relaxation enhancements proves quite beneficial and complementary in approach. Utility of such distance restraints has been exploited before in ferredoxins and other proteins containing paramagnetic moieties (*37*, *39*, *40*, 55); however, this is the first case of application of a hybrid approach combining RDC restraints measured in externally aligned media and paramagnetic distance restraints for determination of high-resolution structures of a [2Fe-2S] ferredoxin in different redox forms. One of the aims of this study was to evaluate the efficacy of such an approach in refining lower resolution structures to higher resolution from homologous structures in paramagnetic [2Fe-2S] ferredoxins. Use of the lower resolution 1PDX structure instead of the higher resolution crystal structures for structure determination of Pdx^r additionally serves the purpose of testing how structurally remote the homologue can be in applying this approach. The fact that our hybrid approach was successful in reproducing most of the structural details inherent in the high-resolution crystal structure and correlating structural properties with dynamic changes in Pdx^r gives rise to the intriguing possibility of using even more remote structural homologues or even modeled ferredoxin structures in future. This augurs well for rapid structure determination of ferredoxins in various redox forms and of paramagnetic proteins in general.

A potential difficulty in application of such an approach would be from lack of sequence-specific assignments in the paramagnetic region. In Pdx, however, this has been overcome previously with rigorous experimental sequence-specific assignments of backbone heteronuclear ^{13}C, ^{15}N resonances via selective decoupling experiments on double-labeled samples. Such a strategy may not be the most efficient strategy for other [2Fe-2S] ferredoxins due to associated costs of preparing a large number of selectively labeled samples and the inherent time involved in making these assignments one at a time. An alternate strategy would be to utilize the assignment scheme based on homologous structure comparisons as suggested by Jain and co-workers (*56*). Paramagnetic restraints in form of distance measurements from relaxation measurements or other restraints such as pseudocontact chemical shifts can then be acquired fairly rapidly for the assigned resonances, allowing structure determination of these regions.

Although the RDC-refined structure of Pdx^o agrees quite well overall with the crystal structures, some differences still remain as discussed in the Results section. The differences are observed due to disorder within the NMR ensemble in some regions of the structure, most notably in the loop region connecting helix D and the metal binding region, as also the loop regions connecting the first two strands, A and B, in the β-sheet. Comparison with dynamics studies indicates the presence of motions, on different time scales, for all of these regions of difference. For Pdx^o, in most regions of the sequence, the crystal structure provides good representation of the average structure in solution. However, even in the crystal structures, the observed RMSD for different independent molecules in the same structure and between different crystal structures is highest for the regions of

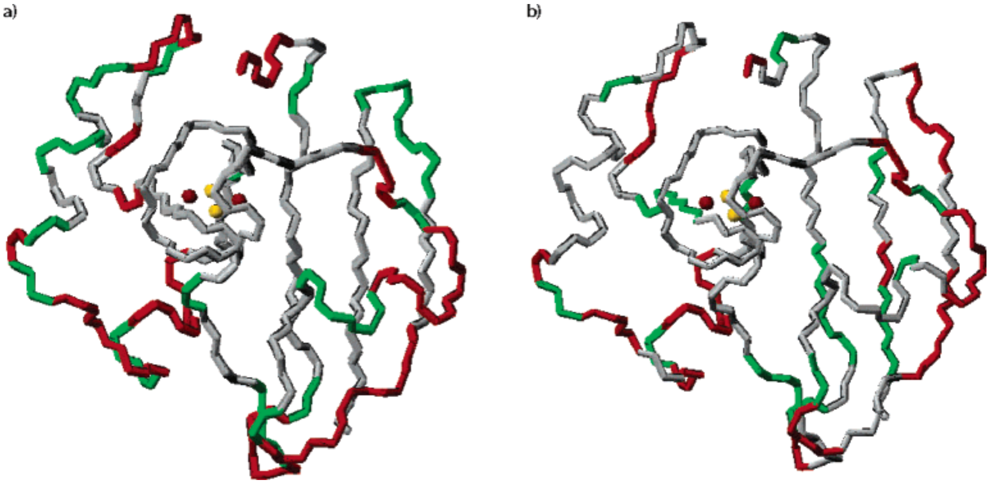

FIGURE 6: Comparison of regions affected due to (a) redox-dependent conformational changes in the backbone structure of Pdx and (b) redox-dependent changes in backbone dynamics (*10*). Residues exhibiting RMSD > 1.6 Å and greatest mobility ($S^2 < 0.89$) are colored in red, while residues exhibiting RMSD in the range 1.2−1.6 Å and moderate mobility ($0.89 > S^2 < 0.93$) are colored in green. The [2Fe-2S] metal cluster is shown as spheres. The figures were prepared using the program MolMol (*64*).

difference due to conformations likely affected by crystal contacts. For these regions, the NMR ensemble reported here may therefore provide a more realistic structural representation in solution.

There is precedent for redox-dependent conformational changes in ferredoxins (*57*−*60*). Like Pdx, in almost all cases, the changes are not dramatic. While redox-dependent dynamical differences have also been observed for these ferredoxins (*61*, *62*), lack of high-resolution structural data in both redox forms has prevented correlation of structural changes to these differences in greater detail. Results from our structure determination for Pdx have allowed us to localize the subtle yet important changes to regions of the protein that have been implicated in functional and dynamic effects previously. The identity of residues deemed to be important in this role from previous NMR and mutagenesis studies has now been confirmed in the present structural study. Reduction of the Fe atom in the metal cluster causes discernible structural effects in the metal binding region that is transmitted through small but distinct changes in the region leading up to the C-terminal cluster. Constriction of the metal binding loop around Cys 39 and Cys 45 would likely pull on adjacent regions through mechanical linkers, such as His 49, that are connected to the metal cluster via a series of hydrogen-bonded and hydrophobic interactions. The primary effect of this would be to cause changes in the regions in its immediate vicinity, such as the region preceding the metal binding loop (Asn 30−Val 36) that would have to undergo an extension to accommodate this change. Part of this extension would come via moving down of helix D on the other end, reducing the overall dynamics of the affected region as has been observed. These structural changes are likely to be transmitted in a secondary manner to the residues in contact with the primarily affected regions (His 8−Gly 11, Val 17−Leu 23). On the C-terminal side, changes in conformation of the metal binding loop might cause the side chain of Ala 46 to move closer to the indole ring of Trp 106, causing its motion to be restricted and reinforcement of the interaction with Val 74. An overall slowing of dynamics would be the likely effect for this region as well. The explanation of structural changes proposed here might thus provide a mechanism to effectively correlate structure with dynamics in a redox-dependent manner. How these structural changes are implied in terms of an electron transfer mechanism though is not clear, except for speculating that the changes would lead to a more favorable orientation of certain residues (e.g., Asp 34, Asp 38) for the binding interaction and electron transfer to CYP101.

It is not hard to rationalize some of the differences observed between solution structures of oxidized and reduced Pdx in terms of a dynamic picture. A hypothesis has been offered by Pochapsky and co-workers to couple conformational changes with changes in dynamics (*23*). According to their model, as a result of decrease in local dynamics, Pdx^r populates a subset of low energy barrier conformational states populated by Pdx^o. The observed structure of Pdx^r would then correspond to a weighted average of the conformational states in this subset, which would be only slightly different from the weighted average of conformational states populated by Pdx^o. In such a case, the observed differences in structure between Pdx^o and Pdx^r are likely to be maximal in the regions affected most by the dynamics and the remaining differences calibrated as a function of the amount of change in dynamics. The fact that we see structural changes as a function of redox state for the very same regions involved in redox-dependent dynamic changes, as shown by a comparison in Figure 6, lends strong credence to this possibility in Pdx. If the subset of conformational states populated by Pdx^r is the same as that populated by Pdx bound to CYP101, then a mechanism for coupling oxidation state to binding affinity is available. There are several lines of experimental evidence to support this. First, the regions affected by changes in dynamics correlate with the regions that change in structure upon change in oxidation state. Second, the correlation of RDCs in the two alignment media is relatively poor in regions known to undergo redox-dependent changes in structure and dynamics as discussed in the Results section. This would indicate motional properties for these regions reflected in the time-averaged RDCs. Third, population of multiple conformational substates by Pdx^o has now been experimentally observed (*23*). Substitution of a flexible residue, Gly 40, in the metal binding loop with a conformationally restrictive residue, Asn, slows down exchange between conformational substates of the dynamic regions adjacent to the metal binding loop in Pdx^o while causing little change in exchange rates of Pdx^r. This implies redox-dependent selection of certain conformational states by Pdx. And, finally, an earlier binding interaction study of Pdx^o with CYP101 identified residues affected by binding that are similar to the residues affected by reduction (*63*). It is highly conceivable that the subset of conformational states populated by Pdx^r is also populated by CYP101-bound Pdx^o, thus reproducing some of the redox-dependent changes upon binding to CYP101. A detailed structural study of the structural changes in Pdx upon binding to CYP101 will have to be carried out to test this further. The hybrid approach employed here for structure determination of Pdx is bound to be quite useful in such an application.

ACKNOWLEDGMENT

The authors thank Diane Slinden and Shawn Leland for assistance with protein purification and data analysis.

SUPPORTING INFORMATION AVAILABLE

A table containing paramagnetic distance restraints used in structure calculation of Pdx^o and Pdx^r, a plot of $^1D_{NH}$ RDC values measured in phage medium versus residue number in Pdx^o and Pdx^r, and a correlation plot of experimental versus back-calculated RDCs in phage medium for Pdx^o and Pdx^r. This material is available free of charge via the Internet at http://pubs.acs.org.

REFERENCES

1. Moleski, C., Moss, T. H., Ormejohn, W. H, and Tsibris, J. C. M. (1970) Magnetic susceptibility of oxidized and reduced iron−sulfur proteins adrenodoxin and putidaredoxin, *Biochim. Biophys. Acta 214*, 548−555.
2. Sligar, S. G., and Gunsalus, I. C. (1976) Thermodynamic model of regulation−modulation of redox equilibria in camphor monoxygenase, *Proc. Natl. Acad. Sci. U.S.A. 73*, 1078−1082.
3. Hintz, M. J., Mock, D. M., Peterson, L. L., Tuttle, K., and Peterson, J. A. (1982) Equilibrium and kinetic-studies of the interaction of cytochrome-P-450cam and putidaredoxin, *J. Biol. Chem. 257*, 4324−4332.
4. Dawson, J. H., Andersson, L. A., and Sono, M. (1982) Spectroscopic investigations of ferric cytochrome P-450-cam ligand complexes−Identification of the ligand trans to cysteinate in the native enzyme, *J. Biol. Chem. 257*, 3606−3617.
5. Sono, M., Andersson, L. A., and Dawson, J. H. (1982) Sulfur donor ligand-binding to ferric cytochrome-P-450-cam and myoglobin−Ultraviolet−visible absorption, magnetic circular-dichroism, and electron-paramagnetic resonance spectroscopic investigation of the complexes, *J. Biol. Chem. 257*, 8308−8320.
6. Unno, M., Christian, J. F., Benson, D., Gerber, N., Sligar, S. G., and Champion, P. M. (1996) Resonance Raman investigations of P450(CAM)/putidaredoxin electron transfer complex, *Biophys. J. 70*, Wp335−Wp335.
7. Reipa, V., Holden, M. J., Mayhew, M. P., and Vilker, V. L. (2000) Temperature dependence of the formal reduction potential of putidaredoxin, *Biochim. Biophys. Acta 1459*, 1−9.
8. Sjodin, T., Christian, J. F., Macdonald, I. D. G., Davydov, R., Unno, M., Sligar, S. C., Hoffman, B. M., and Champion, P. M. (2001) Resonance Raman and EPR investigations of the D251N oxycytochrome p450(cam)/putidaredoxin complex, *Biochemistry 40*, 6852−6859.
9. Tosha, T., Yoshioka, S., Hori, H., Takahashi, S., Ishimori, K., and Morishima, I. (2002) Molecular mechanism of the electron transfer reaction in cytochrome P450(cam)-putidaredoxin: Roles of glutamine 360 at the heme proximal site, *Biochemistry 41*, 13883−13893.
10. Kuznetsov, V. Y., Ivanov, Y. D., Bykov, V. A., Saunin, S. A., Fedorov, I. A., Lemeshko, S. V., Hoa, H. B., and Archakov, A. I. (2002) Atomic force microscopy detection of molecular complexes in multiprotein P450cam containing monooxygenase system, *Proteomics 2*, 1699−1705.
11. Niaura, G., Reipa, V., Mayhew, M. P., Holden, M., and Vilker, V. L. (2003) Structural alterations of the heme environment of cytochrome P450cam and the Y96F mutant as deduced by resonance Raman spectroscopy, *Arch. Biochem. Biophys. 409*, 102−112.
12. Nagano, S., Shimada, H., Tarumi, A., Hishiki, T., Kimata-Ariga, Y., Egawa, T., Suematsu, M., Park, S. Y., Adachi, S., Shiro, Y., and Ishimura, Y. (2003) Infrared spectroscopic and mutational studies on putidaredoxin-induced conformational changes in ferrous CO-P450cam, *Biochemistry 42*, 14507−14514.
13. Nagano, S., Tosha, T., Ishimori, K., Morishima, I., and Poulos, T. L. (2004) Crystal structure of the cytochrome P450cam mutant that exhibits the same spectral perturbations induced by putidaredoxin binding, *J. Biol. Chem. 279*, 42844−42849.
14. Purdy, M. M., Koo, L. S., de Montellano, P. R. O., and Klinman, J. P. (2004) Steady-state kinetic investigation of cytochrome P450cam: Interaction with redox partners and reaction with molecular oxygen, *Biochemistry 43*, 271−281.
15. Lipscomb, J. D., Sligar, S. G., Namtvedt, M. J., and Gunsalus, I. C. (1976) Autooxidation and hydroxylation reactions of oxygenated cytochrome P-450cam, *J. Biol. Chem. 251*, 1116−1124.
16. Ormejohnson, N. R., Mims, W. B., Ormejohnson, W. H., Bartsch, R. G., Cusanovich, M. A., and Peisach, J. (1983) Oxidation-state dependence of proton-exchange near the iron−sulfur centers in ferredoxins and high-potential iron−sulfur proteins, *Biochim. Biophys. Acta 748*, 68−72.
17. Ratnaswamy, G., and Pochapsky, T. C. (1993) Characterization of hyperfine-shifted H-1 resonances in oxidized and reduced putidaredoxin, an Fe2s2 ferredoxin from *Pseudomonas putida*, *Magn. Reson. Chem. 31*, S73−S77.
18. Pochapsky, T. C., Ratnaswamy, G., and Patera, A. (1994) Redox-dependent H-1-NMR spectral features and tertiary structural constraints on the C-terminal region of putidaredoxin, *Biochemistry 33*, 6433−6441.
19. Lyons, T. A., Ratnaswamy, G., and Pochapsky, T. C. (1996) Redox-dependent dynamics of putidaredoxin characterized by amide proton exchange, *Protein Sci. 5*, 627−639.
20. Sari, N., Holden, M. J., Mayhew, M. P., Vilker, V. L., and Coxon, B. (1999) Comparison of backbone dynamics of oxidized and reduced putidaredoxin by N-15 NMR relaxation measurements, *Biochemistry 38*, 9862−9871.
21. Shimada, H., Nagano, S., Ariga, Y., Unno, M., Egawa, T., Hishiki, T., and Ishimura, Y. (1999) Putidaredoxin-cytochrome P450(cam) interaction−Spin state of the heme iron modulates putidaredoxin structure, *J. Biol. Chem. 274*, 9363−9369.
22. Mukhopadhyay, R., Wong, L. L., Lo, K. K., Pochapsky, T., and Hill, H. A. O. (2002) A molecular level study of complex formation between putidaredoxin and cytochrome P450 by scanning tunnelling microscopy, *Phys. Chem. Chem. Phys. 4*, 641−646.
23. Pochapsky, T. C., Kostic, M., Jain, N., and Pejchal, R. (2001) Redox-dependent conformational selection in a Cys(4)Fe(2)S(2) ferredoxin, *Biochemistry 40*, 5602−5614.
24. Pochapsky, T. C., Ye, X. M., Ratnaswamy, G., and Lyons, T. A. (1994) An NMR-derived model for the solution structure of oxidized putidaredoxin, a 2-Fe, 2-S ferredoxin from *Pseudomonas*, *Biochemistry 33*, 6424−6432.
25. Pochapsky, T. C., Jain, N. U., Kuti, M., Lyons, T. A., and Heymont, J. (1999) A refined model for the solution structure of oxidized putidaredoxin, *Biochemistry 38*, 4681−4690.
26. Muller, A., Muller, J. J., Muller, Y. A., Uhlmann, H., Bernhardt, R., and Heinemann, U. (1998) New aspects of electron transfer revealed by the crystal structure of a truncated bovine adrenodoxin, Adx(4−108), *Structure 6*, 269−280.
27. Sevrioukova, I. F., Garcia, C., Li, H. Y., Bhaskar, B., and Poulos, T. L. (2003) Crystal structure of putidaredoxin, the [2Fe-2S] component of the P450cam monooxygenase system from *Pseudomonas putida*, *J. Mol. Biol. 333*, 377−392.
28. Smith, N., Mayhew, M., Holden, M. J., Kelly, H., Robinson, H., Heroux, A., Vilker, V. L., and Gallagher, D. T. (2004) Structure of C73G putidaredoxin from *Pseudomonas putida*, *Acta Crystallogr. D 60*, 816−822.
29. Tjandra, N., and Bax, A. (1997) Direct measurement of distances and angles in biomolecules by NMR in a dilute liquid crystalline medium, *Science 278*, 1111−1114.
30. Clore, G. M., Gronenborn, A. M., and Tjandra, N. (1998) Direct structure refinement against residual dipolar couplings in the presence of rhombicity of unknown magnitude, *J. Magn. Reson. 131*, 159−162.

31. Fischer, M. W. F., Losonczi, J. A., Weaver, J. L., and Prestegard, J. H. (1999) Domain orientation and dynamics in multidomain proteins from residual dipolar couplings, *Biochemistry 38*, 9013−9022.
32. Clore, G. M. (2000) Accurate and rapid docking of protein−protein complexes on the basis of intermolecular nuclear Overhauser enhancement data and dipolar couplings by rigid body minimization, *Proc. Natl. Acad. Sci. U.S.A. 97*, 9021−9025.
33. Hus, J. C., Marion, D., and Blackledge, M. (2000) De novo determination of protein structure by NMR using orientational and long-range order restraints, *J. Mol. Biol. 298*, 927−936.
34. Tian, F., Valafar, H., and Prestegard, J. H. (2001) A dipolar coupling based strategy for simultaneous resonance assignment and structure determination of protein backbones, *J. Am. Chem. Soc. 123*, 11791−11796.
35. Jain, N. U., Noble, S., and Prestegard, J. H. (2003) Structural characterization of a mannose-binding protein-trimannoside complex using residual dipolar couplings, *J. Mol. Biol. 328*, 451−462.
36. Lee, Y. M., Arnesano, F., Banci, L., Barbieri, R., Bertini, I., Felli, I., Luchinat, C., Piccioli, M., Sarrou, J., and Rosato, A. (2001) Self-orientation of paramagnetic molecules in high magnetic fields for structure determination, *J. Inorg. Biochem. 86*, 504.
37. Parigi, G., Bertini, I., Luchinat, C., Piccioli, M., and Piva, A. (2001) Paramagnetic constraints in structure-determination programs, *J. Inorg. Biochem. 86*, 507.
38. Barbieri, R., Bertini, I., Cavallaro, G., Lee, Y. M., Luchinat, C., and Rosato, A. (2002) Paramagnetically induced residual dipolar couplings for solution structure determination of lanthanide binding proteins, *J. Am. Chem. Soc. 124*, 5581−5587.
39. Bertini, I., Donaire, A., Luchinat, C., and Rosato, A. (1997) Paramagnetic relaxation as a tool for solution structure determination: *Clostridium pasteurianum* ferredoxin as an example, *Proteins 29*, 348−358.
40. Bertini, I., Luchinat, C., and Rosato, A. (1996) The solution structure of paramagnetic metalloproteins, *Prog. Biophys. Mol. Biol. 66*, 43−80.
41. Jain, N. U., and Pochapsky, T. C. (1998) Redox dependence of hyperfine-shifted C-13 and N-15 resonances in putidaredoxin, *J. Am. Chem. Soc. 120*, 12984−12985.
42. Palmer, A. G., Cavanagh, J., Wright, P. E., and Rance, M. (1991) Sensitivity Improvement in proton-detected 2-dimensional heteronuclear correlation NMR-spectroscopy, *J. Magn. Reson. 93*, 151−170.
43. Schwieters, C. D., Kuszewski, J. J., Tjandra, N., and Clore, G. M. (2003) The XPLOR-NIH NMR molecular structure determination package, *J. Magn. Reson. 160*, 65−73.
44. Dosset, P., Hus, J. C., Marion, D., and Blackledge, M. (2001) A novel interactive tool for rigid-body modeling of multi-domain macromolecules using residual dipolar couplings, *J. Biomol. NMR 20*, 223−231.
45. Chou, J. J., Li, S. P., and Bax, A. (2000) Study of conformational rearrangement and refinement of structural homology models by the use of heteronuclear dipolar couplings, *J. Biomol. NMR 18*, 217−227.
46. Laskowski, R. A., Rullmann, J. A. C., MacArthur, M. W., Kaptein, R., and Thornton, J. M. (1996) AQUA and PROCHECK-NMR: Programs for checking the quality of protein structures solved by NMR, *J. Biomol. NMR 8*, 477−486.
47. Pochapsky, T. C., Kuti, M., and Kazanis, S. (1998) The solution structure of a gallium-substituted putidaredoxin mutant: GaPdx C85S, *J. Biomol. NMR 12*, 407−415.
48. Kostic, M., Bernhardt, R., and Pochapsky, T. C. (2003) A conserved histidine in vertebrate-type ferredoxins is critical for redox-dependent dynamics, *Biochemistry 42*, 8171−8182.
49. Davies, M. D., and Sligar, S. G. (1992) Genetic-variants in the putidaredoxin cytochrome-P-450(Cam) electron transfer complex−Identification of the residue responsible for redox-state-dependent conformers, *Biochemistry 31*, 11383−11389.
50. Stayton, P. S., and Sligar, S. G. (1991) Structural microheterogeneity of a tryptophan residue required for efficient biological electron transfer between putidaredoxin and cytochrome-P-450cam, *Biochemistry 30*, 1845−1851.
51. Holden, M., Mayhew, M., Bunk, D., Roitberg, A., and Vilker, V. (1997) Probing the interactions of putidaredoxin with redox partners in camphor p450 5-monooxygenase by mutagenesis of surface residues, *J. Biol. Chem. 272*, 21720−21725.
52. Schwalbe, H., Grimshaw, S. B., Spencer, A., Buck, M., Boyd, J., Dobson, C. M., Redfield, C., and Smith, L. J. (2001) A refined solution structure of hen lysozyme determined using residual dipolar coupling data, *Protein Sci. 10*, 677−688.
53. Zheng, D. Y., Aramini, J. M., and Montelione, G. T. (2004) Validation of helical tilt angles in the solution NMR structure of the Z domain of staphylococcal protein A by combined analysis of residual dipolar coupling and NOE data, *Protein Sci. 13*, 549−554.
54. Stauffer, M. E., Skelton, N. J., and Fairbrother, W. J. (2002) Refinement of the solution structure of the heparin-binding domain of vascular endothelial growth factor using residual dipolar couplings, *J. Biomol. NMR 23*, 57−61.
55. Bertini, I., Couture, M. M. J., Donaire, A., Eltis, L. D., Felli, I. C., Luchinat, C., Piccioli, M., and Rosato, A. (1996) The solution structure refinement of the paramagnetic reduced high-potential iron−sulfur protein I from *Ectothiorhodospira halophila* by using stable isotope labeling and nuclear relaxation, *Eur. J. Biochem. 241*, 440−452.
56. Jain, N. U., and Pochapsky, T. C. (1999) A new assignment strategy for the hyperfine-shifted C-13 and N-15 resonances in Fe2S2 ferredoxins, *Biochem. Biophys. Res. Commun. 258*, 54−59.
57. Xia, B., Volkman, B. F., and Markley, J. L. (1998) Evidence for oxidation-state-dependent conformational changes in human ferredoxin from multinuclear, multidimensional NMR spectroscopy, *Biochemistry 37*, 3965−3973.
58. Dugad, L. B., Lamar, G. N., Banci, L., and Bertini, I. (1990) Identification of localized redox states in plant-type 2-iron ferredoxins using the nuclear Overhauser effect, *Biochemistry 29*, 2263−2271.
59. Beilke, D., Weiss, R., Lohr, F., Pristovsek, P., Hannemann, F., Bernhardt, R., and Ruterjans, H. (2002) A new electron transport mechanism in mitochondrial steroid hydroxylase systems based on structural changes upon the reduction of adrenodoxin, *Biochemistry 41*, 7969−7978.
60. Wilkens, S. J., Xia, B., Weinhold, F., Markley, J. L., and Westler, W. M. (1998) NMR investigations of *Clostridium pasteurianum* rubredoxin. Origin of hyperfine H-1, H-2, C-13 and N-15 NMR chemical shifts in iron−sulfur proteins as determined by comparison of experimental data with hybrid density functional calculations, *J. Am. Chem. Soc. 120*, 4806−4814.
61. Dangi, B., Blankman, J. I., Miller, C. J., Volkman, B. F., and Guiles, R. D. (1998) Contribution of backbone dynamics to entropy changes occurring on oxidation of cytochrome b(5). Can redox linked changes in hydrogen bond networks modulate reduction potentials?, *J. Phys. Chem. B 102*, 8201−8208.
62. Muller, J. J., Muller, A., Rottmann, M., Bernhardt, R., and Heinemann, U. (1999) Vertebrate-type and plant-type ferredoxins: Crystal structure comparison and electron transfer pathway modelling, *J. Mol. Biol. 294*, 501−513.
63. Pochapsky, T. C., Lyons, T. A., Kazanis, S., Arakaki, T., and Ratnaswamy, G. (1996) A structure-based model for cytochrome P450(cam)-putidaredoxin interactions, *Biochimie 78*, 723−733.
64. Koradi, R., Billeter, M., and Wuthrich, K. (1996) MOLMOL: A program for display and analysis of macromolecular structures, *J. Mol. Graphics 14*, 51−55.
65. Sayle, R. A., and Milnerwhite, E. J. (1995) Rasmol−Biomolecular graphics for all, *Trends Biochem. Sci. 20*, 374−376.
66. Sevrioukova, I. F. (2005) Redox-dependent structural reorganization in putidaredoxin, a vertebrate-type [2Fe-2S] ferredoxin from *Pseudomonas putida*, *J. Mol. Biol. 347*, 607−621.

BI050152C